Journal of Fluids and Structures 123 (2023) 103987

Contents lists available at ScienceDirect

Journal of Fluids and Structures

journal homepage: www.elsevier.com/locate/jfs

Scaling approaches and scale effects in wave–flexible structure interaction

Tommaso Attili [a,*], Valentin Heller [a], Savvas Triantafyllou [b]

[a] Environmental Fluid Mechanics and Geoprocesses Research Group, Faculty of Engineering, University of Nottingham, Nottingham NG7 2RD, UK

[b] Institute for Structural Analysis and Aseismic Research, School of Civil Engineering, National Technical University of Athens, Athens, Greece

ARTICLE INFO

Keywords:
Breaking waves
Laboratory experiments
Numerical modelling
Scale effects
Similarity
Wave–flexible structure interaction

ABSTRACT

Laboratory models are important for research, to inform design solutions and to calibrate and validate numerical models. Unfortunately, model-prototype similarity is often difficult to achieve in small models, resulting in scale effects. For Wave–Flexible Structure Interaction (WFSI), scale effects arise when the fluid and/or structure properties are incorrectly scaled. The present study provides a systematic investigation of scale effects for wave impacts on flexible and rigid plates based on numerical modelling supported by small-scale laboratory tests. Non-breaking and breaking wave impacts were simulated with regular and solitary waves for the prototypes and up to 40 times smaller models. These were scaled according to the scaling approaches (i) precise Froude (fluid and plate properties scaled), (ii) traditional Froude–Cauchy (fluid properties unscaled, plate properties scaled), (iii) traditional Froude (fluid and plate properties unscaled) and (iv) a new WFSI approach (partial conservation of the WFSI governing parameters). The numerical results confirmed the absence of scale effects for (i). Non-breaking wave impacts were correctly predicted for (ii), however, up to 132% scale effects were observed in the breaking wave pressures due to the unscaled fluid properties. The plate displacements were underestimated by up to 98% for (iii). The new approach (iv) was successfully validated based on non-breaking waves, with less than 4.3% deviations for the maximum regular wave forces and plate displacements. Additionally, less than 3% deviations for the maximum solitary wave force and plate displacement were observed. The new scaling approach provides a more versatile alternative to traditional Froude–Cauchy scaling laws to support laboratory investigations of WFSI.

1. Introduction

1.1. Background

Wave–Structure Interaction (WSI) is relevant for numerous coastal and offshore structures, including breakwaters, floating and bottom-fixed wind turbines, wave energy converters and offshore oil and gas platforms (Cuomo et al., 2010a; He and Kashiwagi, 2012; Didier et al., 2014). For flexible structures undergoing non-negligible displacements, i.e. deflections larger than 0.5 to 2.0% of the structure length, called Wave-Flexible Structure Interaction (WFSI) herein, the involved physical processes are

* Corresponding author.
E-mail addresses: tommasoattili4@gmail.com (T. Attili), valentin.heller@nottingham.ac.uk (V. Heller), savtri@mail.ntua.gr (S. Triantafyllou).

https://doi.org/10.1016/j.jfluidstructs.2023.103987
Received 14 April 2023; Received in revised form 23 July 2023; Accepted 14 September 2023
Available online 5 October 2023

Notation

a	Wave amplitude, m
b	Plate width, m
Ba	Bagnold number
C	Courant number
$C_{B\text{-}M}$	Constant in the Bagnold–Mitsuyasu scaling law
c_{sound}	Speed of sound in air, m/s
Ca	Cauchy number
$\mathbf{D}_F$	Deformation gradient
D	Plate flexural rigidity in 2D, N m
D_{3D}	Plate flexural rigidity in 3D, N m^2
$\mathbf{d}$	Displacement vector, m
d_x	Plate displacement component along x-axis, m
E	Young's modulus, N/m^2
F	Force on plate per unit width, N/m
F_{3D}	Force on plate, N
f_σ	Surface tension force per unit volume, N/m^3
Fr	Froude number
$\mathbf{g}$	Gravitational acceleration vector, m/s^2
g	Gravitational acceleration, m/s^2
H	Wave height, m
h	Water depth, m
I	Identity matrix
J	Determinant of $\mathbf{D}_F$
K	Bulk modulus, N/m^2
k	Turbulent kinetic energy, m^2/s^2
l	Plate height, m
M_s	Mass per unit area, kg/m^2
$M_{3D,s}$	Mass per unit length, kg/m
Ma	Mach number
p	Pressure, N/m^2
$\bar{p}$	Mean pressure, N/m^2
p_0	Atmospheric pressure, N/m^2
R^2	Coefficient of determination
Re	Reynolds number
s	Plate thickness, m
T	Wave period, s
T_s	Natural period of the plate, s
t	Time, s
$\bar{\mathbf{u}}$	Mean fluid velocity vector, m/s
$\overline{\mathbf{u}'\mathbf{u}'}$	Turbulent stress tensor, N/m^2
u	Fluid velocity, m/s
$\bar{u}_x, \bar{u}_y, \bar{u}_z$	Mean fluid velocity component along x-, y- and z-axis, m/s
We	Weber number
x, y, z	x-, y- and z-axis, m
α	Fraction of volume
β	Plate inclination, °
Δd_x	Scale effects for the horizontal plate displacement, %
ΔF	Scale effects for the force on the plate, %
Δt	Time step, s
$\Delta x, \Delta y, \Delta z$	Cell sizes, m

$\Delta\lambda_p$	Deviation between the predicted and numerical pressure scaling law, %
ε	Turbulence energy dissipation rate, m^2/s^3
ε_{zz}	Strain component of the plate along z-axis
η	Water surface elevation, m
λ	Geometrical scale factor
λ_E	Young's modulus scaling law
λ_p	Pressure scaling law
μ	Fluid dynamic viscosity, N s/m^2
ν	Fluid kinematic viscosity, m^2/s
Π_1 to Π_7	Dimensionless governing parameters for WFSI
π	Mathematical constant
ρ	Density, kg/m^3
σ	Surface tension, N/m
$\boldsymbol{\sigma}_s$	Stress tensor, N/m^2
σ_{zz}	Normal plate stress component along z-axis, N/m^2

Subscripts

a	Air
d	Downwave
H	Horizontal
M	Model
max	Maximum
num	Numerical
P	Prototype
$pred$	Predicted
s	Structure, solid
u	Upwave
w	Water

Abbreviations

CFL	Courant–Friedrichs–Lewy
CPU	Central Processing Unit
FE 4.0	Foam-Extend 4.0
FVM	Finite Volume Method
GP	New scaling approach based on the WFSI Governing Parameters
HPC	High Performance Computing
LC	Load Cell
PFr	Precise Froude scaling
PPT	Precision Pressure Transducer
RANS	Reynolds-Averaged Navier–Stokes
SG	Strain Gauge
TFr	Traditional Froude scaling
TFr_E	Traditional Froude–Cauchy scaling
VOF	Volume Of Fluid
WFSI	Wave–Flexible Structure Interaction
WG	Wave Gauge
WSI	Wave–Structure Interaction
2D	Two-Dimensional (flume)
3D	Three-Dimensional (basin)

particularly complex. These structures may suffer from large stresses and deformations under wave loading and experience damage under extreme conditions. Given the complexity of these processes, e.g. variable geometries and complex flow fields, laboratory models (Linton et al., 2013; Krautwald et al., 2022; Attili et al., 2023) are often used for research, to inform design solutions and to calibrate and validate numerical simulations.

A laboratory model is similar to its prototype if geometric, kinematic and dynamic similarities are satisfied (Kobus, 1980; Hughes, 1993; Heller, 2011). Exact model-prototype similarity is rarely achieved, due to the challenge of keeping all relevant force ratios constant between the prototype and its model. This results in scale effects, manifesting themselves in a variety of ways. For example, they can result in considerably different void fractions in air–water flows (Catucci et al., 2021) or non-identical pressures and forces in WSI between a model and its prototype (Abrahamsen and Faltinsen, 2013; Bredmose et al., 2015).

Free-surface flow models are commonly scaled according to the Froude scaling laws (Le Méhauté, 1976; Hughes, 1993; Heller, 2011; Sheng et al., 2014), ensuring the same Froude number Fr = (inertial force/gravity force)$^{1/2}$ in the prototype and model. When ordinary water and air are used in the model, other force ratios, such as the Reynolds number (inertial force/viscous force)

$$\mathrm{Re} = \frac{g^{1/2}h^{3/2}}{\nu} \tag{1}$$

and Weber number (inertial force/surface tension force)

$$\mathrm{We} = \frac{\rho_w g h^2}{\sigma} \tag{2}$$

are not conserved, introducing scale effects. In Eqs. (1) and (2), the shallow-water wave speed $(gh)^{1/2}$ was used as the characteristic velocity, with the gravitational acceleration g and the water depth h. The characteristic velocity and length can change with the investigated phenomenon. Further, ν is the kinematic viscosity, ρ_w the water (subscript w) density and σ the surface tension.

Re and We play a key role for air–water flows, e.g. for breaking waves (Kiger and Duncan, 2012) and plunging jets (Chanson et al., 2004; Catucci et al., 2021). Furthermore, the Mach number Ma = (inertial force/compressibility force) can be relevant when the air–water flow compressibility is important, e.g. for oscillating water columns (Falcão and Henriques, 2014) and violent wave impacts (Bredmose et al., 2015). For such processes, the Froude scaling laws typically provide unsatisfactory predictions (Hughes, 1993; Heller, 2011).

In WSI, scale effects are generally negligible for non-breaking waves under Froude similarity for commonly used laboratory scales, i.e. 1:10 to 1:50 (Hughes, 1993; Cuomo et al., 2010b). However, relevant scale effects are observed for breaking wave impacts (Hughes, 1993; Cuomo et al., 2010b; Blenkinsopp and Chaplin, 2011; Martinelli et al., 2011; Bredmose et al., 2015). Cuomo et al. (2010b) suggested an approach to remove scale effects in the upscaling process of wave impact pressures on rigid walls. Their approach provides an estimate of the corrected pressure scaling law λ_p based on the Bagnold number Ba. This is a measure of the peak impact pressure and was expressed as (Cuomo et al., 2010b)

$$\mathrm{Ba} = \frac{0.2(1-\pi/12)}{\pi/12}\frac{\rho_w g(h+H)}{p_0}, \tag{3}$$

with the wave height H and the atmospheric pressure p_0. Cuomo et al. (2010b) revealed that wave impact pressures on rigid coastal structures are overestimated by the Froude scaling laws. This was confirmed numerically by Bredmose et al. (2015), who found larger pressures in smaller models due to the relatively stiffer air. To overcome this, Bredmose et al. (2015) recommended to use the Bagnold–Mitsuyasu law for pressures larger than 3.18 times the atmospheric pressure, whilst for smaller pressures the Froude scaling laws provide good predictions. However, none of the aforementioned studies took potential structural deformations into account.

In WFSI, the geometry and elastic properties of the structure must also be appropriately scaled (Hudson et al., 1979; Hughes, 1993; Chakrabarti, 2005; Heller, 2011; Martinelli et al., 2011; Krautwald et al., 2022; Abrahamsen et al., 2023; Lambert et al., 2023). When elastic forces are relevant, scaling criteria follow the Cauchy similarity based on the Cauchy number Ca = (inertial force/elastic force). Froude and Cauchy similarities can be combined to the Froude–Cauchy similarity for WFSI phenomena (Le Méhauté, 1965; Chakrabarti, 2005; Krautwald et al., 2022), in which the Young's modulus E is scaled linearly with the geometrical scale factor between the prototype (subscript P) and model (subscript M) (Le Méhauté, 1965)

$$\lambda = \frac{h_P}{h_M}. \tag{4}$$

As the structure (subscript s) density ρ_s and Poisson ratio have to be constant between the prototype and its model, it is challenging to find an appropriate material for small scales. On the other hand, an incorrect scaling of the structural properties may have disastrous consequences, as in the case of the Sines breakwater which failed in 1978, partially due to an underdesign informed by misleading laboratory results (Oumeraci, 1984; Le Méhauté, 1990). The most relevant WSI scaling studies are summarised in Table 1.

A systematic investigation of scale effects in WFSI, including the modelling of both the fluid and the structure, is still lacking. The present study explores scale effects in wave impacts on rigid and flexible plates based on numerical modelling supported by small-scale laboratory experiments (Appendix B). Dimensionless governing parameters are validated and used to define a new scaling approach which is more versatile than Froude–Cauchy scaling. Scale effects are systematically quantified for a range of scaling approaches to illustrate the benefits of this new approach.

Table 1
Relevant scaling studies for various WSI phenomena.

Reference	Investigated phenomenon	λ	Comment
Cuomo et al. (2010b)	Wave impact pressures on vertical walls	1 to 40	Approach to upscale breaking wave pressures by removing scale effects
Abrahamsen and Faltinsen (2013)	Entrapped air pockets during slamming events	1 to 1200	New scaling laws for gas pocket pressures and rise times
Bredmose et al. (2015)	Breaking wave impacts on walls	1/16 to 16	New scaling law for breaking wave pressures
Catucci et al. (2021)	Dam break waves impacting an obstacle	1 to 16	Novel scaling laws excluding scale effects in air–water flows
Krautwald et al. (2022)	Bore wave impacts on (collapsing) timber structures	5	Large-scale experimental model under Froude–Cauchy similarity

1.2. Aims and structure

The present study is aimed at:

- Formulating and validating a set of governing parameters fully representing the underlying physics of WFSI.
- Formulating a new scaling approach for WFSI.
- Investigating scale effects in WSI based on different scaling approaches.

The remainder of this article is organised as follows. In Section 2, the numerical model is presented, including the governing equations and the numerical set-ups. This is followed by the governing parameters for WFSI, along with traditional scaling laws and the new scaling approach. The main results are presented in Section 3, including the validation of the governing parameters and scale effects. These findings are discussed and applied to upscale new laboratory measurements in Section 4 and the main conclusions are summarised in Section 5. The appendices include the convergence tests (Appendix A), a description of the physical experiments along with the main laboratory results (Appendix B), used as illustrative examples for discussing scale effects and upscaling the results to hypothetical prototype scales, and additional data about the scaling and scale effects (Appendix C).

2. Methodology

2.1. Numerical model

2.1.1. Governing equations and coupling technique

The open source toolbox solids4foam (Cardiff et al., 2018; Attili et al., 2021; 2022; 2023), implemented in foam-extend 4.0 (FE 4.0) (OpenFOAM extension, 2016), was used in the present study. The fluid and solid domains were solved based on the Finite Volume Method (FVM) discretisation and coupled with a partitioned approach. An incompressible Newtonian fluid model was used, satisfying the continuity

$$\nabla \cdot \bar{\mathbf{u}} = 0 \tag{5}$$

and Reynolds-Averaged Navier–Stokes (RANS) equations

$$\frac{\rho \partial \bar{\mathbf{u}}}{\partial t} + \rho(\bar{\mathbf{u}} \cdot \nabla)\bar{\mathbf{u}} = -\nabla \bar{p} + \rho \nabla \cdot (\mu \nabla \cdot \bar{\mathbf{u}} - \overline{\mathbf{u}'\mathbf{u}'}) + \rho \mathbf{g} + f_\sigma. \tag{6}$$

In Eqs. (5) and (6), $\bar{\mathbf{u}} = (\bar{u}_x, \bar{u}_y, \bar{u}_z)$ is the mean fluid velocity vector, $\bar{p}$ the mean pressure, μ the fluid dynamic viscosity, $\overline{\mathbf{u}'\mathbf{u}'}$ the turbulent stress tensor, t the time, $\mathbf{g}$ the gravitational acceleration vector and f_σ the surface tension force per unit volume (Brackbill et al., 1992). The k-ϵ turbulence model (Launder and Spalding, 1974) was used.

The time integration of Eqs. (5) and (6) was controlled based on the Courant–Friedrichs–Lewy (CFL) convergence condition (Courant et al., 1928)

$$C = \frac{\bar{u}_x \Delta t}{\Delta x} + \frac{\bar{u}_y \Delta t}{\Delta y} + \frac{\bar{u}_z \Delta t}{\Delta z} \leq 1 \tag{7}$$

where C is the Courant number, Δt the time step and Δx, Δy and Δz are the cell sizes in the x, y and z direction, respectively. Eqs. (5) and (6) were complemented with the Volume Of Fluid (VOF) method (Hirt and Nichols, 1981) to model air–water flows. This is based on the fraction of volume α, which varies from 0 to 1, with $\alpha = 0$ denoting air, $\alpha = 1$ water and $\alpha = 0.5$ was used to track the air–water interface. The wave generation and absorption was performed with the toolbox waves2Foam (Jacobsen et al., 2012), using a relaxation zone of 3 times the wave length L.

Contrary to the fluid, a Lagrangian approach was adopted for the solid domain. The momentum equation

$$\rho_s \frac{\partial^2 \mathbf{d}_s}{\partial t^2} + \nabla \cdot [(J\mathbf{D}_F^{-T}) \cdot \boldsymbol{\sigma}_s] = \rho_s \mathbf{g} \tag{8}$$

was solved, assuming large displacement kinematics with the Neo-Hookean elastic constitutive law. In Eq. (8), $\mathbf{d}_s$ is the solid (subscript s) displacement vector, ρ_s the solid density, $\mathbf{D}_F = \mathrm{I} + (\nabla \mathbf{d}_s)^T$ the deformation gradient, with the identity matrix I, J the determinant of $\mathbf{D}_F$ and $\boldsymbol{\sigma}_s$ the stress tensor in Voigt notation.

The fluid–solid coupling was carried out with a partitioned approach (Tuković et al., 2018; Liu and Zhang, 2019). As such, after solving the fluid velocity and pressure fields, the fluid forces acting on the solid were evaluated. These were used as new boundary conditions to update the solid domain. Consequently, the new solid velocities were transferred to the fluid and the fluid mesh was updated. This was performed in a loop within each time step until convergence was achieved (Cardiff et al., 2018). This numerical model resulted in an overall good agreement with laboratory measurements for wave impacts on rigid and flexible plates (Attili et al., 2023).

2.1.2. Numerical set-up and test programme

The numerical set-up involved a wave flume (2D) with a vertical offshore plate, as shown in Fig. 1a. Cartesian coordinates (x, y, z) are used in this study, with the origin at the still water surface. The plate, with $\rho_s = 8000$ kg/m^3 and $E = 200$ GPa, is 10 m high with a constant thickness $s = 0.15$ m. Similarly as in Attili et al. (2023), this design was inspired by the flood protection system MOSE (Erbisti, 2014) and the Oyster wave energy converter (Lagoun et al., 2010). A Poisson ratio of 0.3 was used in all tests.

A total of 3 prototype simulation tests have been conducted, involving non-breaking regular and solitary waves with the values for the wave height H, period T and amplitude a shown in Table 2. The simulations were run on the High Performance Computing (HPC) cluster Augusta at the University of Nottingham with 60 Central Processing Units (CPUs) and 150 GB of memory. A fluid resolution of $\Delta x = \Delta z = 0.05$ m was employed in a 11.00 m × 20.00 m refined area, with $\Delta x = \Delta z = 0.10$ m in the remainder of the domain (Fig. 1, Appendix A). A solid resolution of $\Delta x = \Delta z = 0.017$ m was used. The simulations were conducted with a fixed $\Delta t = 0.025$ s for the regular and $\Delta t = 0.017$ s for the solitary wave tests, satisfying Eq. (7). The regular wave tests took up to 50 h to simulate 102 s and a solitary wave test took approximately 20 h to simulate 20 s.

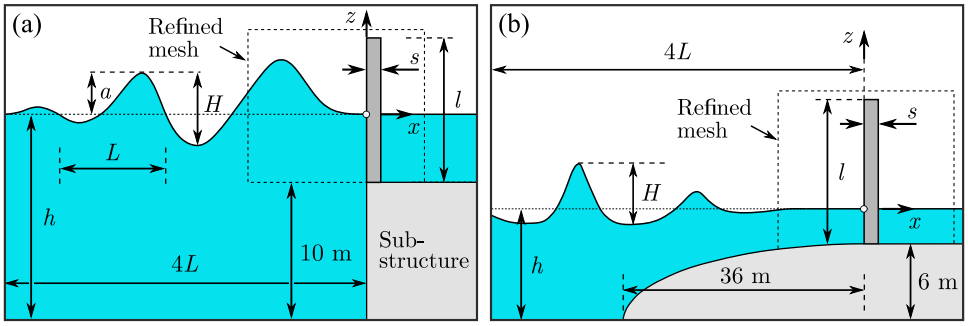

Fig. 1. Side view of the prototype numerical set-ups for the (a) non-breaking wave and (b) breaking wave tests.

Table 2
Test programme for the prototype numerical tests.

Parameter	Symbol	Unit	Non-breaking waves	Breaking waves
Water depth	h	m	15	8.5
Plate height	l	m	10	10
Young's modulus	E	GPa	200	200, 400
Plate thickness	s	m	0.15	0.15, 0.50
Plate density	ρ_s	kg/m^3	8000	8000
Regular waves	H	m	2	2.90
	H/h	–	0.13	0.34
	T	s	5.5, 11	11.30
	$T(g/h)^{1/2}$	–	4.45, 8.90	12.14
Solitary waves	a	m	2	–
	a/h	–	0.13	–

2.1.3. Numerical simulation of breaking waves impacting plates

Additional numerical tests have been conducted to investigate breaking wave impacts on a plate. The numerical set-up was inspired by Bredmose et al. (2015), consisting of a wave flume with the plate located on top of a semi-elliptical shore (Fig. 1b). The 2 prototype tests involved a regular wave with $H = 2.9$ m and $T = 11.3$ s at $h = 8.5$ m, impacting a rigid and flexible plate with their mechanical properties summarised in Table 2. The same mesh resolution as for the tests in Section 2.1.2 was employed, with an adaptive Δt. Simulations were run on the HPC, taking up to 3.5 days to simulate 73 s.

Table 3
Dimensionless governing parameters in 2D WFSI.

Π_1	Π_2	Π_3	Π_4	Π_5	Π_6	Π_7
$\frac{H}{h}$	$T\left(\frac{g}{h}\right)^{1/2}$	$\frac{\nu}{g^{1/2}h^{3/2}}$	$\frac{\sigma}{\rho_w g h^2}$	$\frac{M_s}{\rho_w h}$	$\frac{D}{\rho_w g h^4}$	$\frac{l}{h}$

2.2. Governing parameters in WFSI

For 2D wave interactions with flexible plates, 10 governing parameters were identified: H, T, h, ρ_w, ν, σ, the plate flexural rigidity $D = Es^3/12$, the plate mass per unit area $M_s = \rho_s s$, l and g. These involve the 3 units length [L], mass [M] and time [T], i.e. they can be reduced to a set of 7 dimensionless quantities based on the 3 reference parameters ρ_w, h and g (Buckingham, 1914). This results in the 7 dimensionless quantities shown in Table 3. Π_1 to Π_4 include the fluid parameters, with Π_1 and Π_2 representing the dimensionless wave height and period, and Π_3 and Π_4 the inverse of Re and We, respectively. The plate parameters are included in Π_5 to Π_7, resulting in the relative mass (Π_5), stiffness (Π_6) and height (Π_7). These dimensionless quantities can be used for a general dimensionless presentation of results without the need for upscaling (Section 3.1).

2.3. Scaling approaches

The prototype tests (Table 2) have been simulated within a scale series (Heller et al., 2008) based on 4 different scaling approaches. These are summarised in Table 4 with the corresponding scaling laws for all relevant parameters. Simulations with geometrical scale factors $\lambda = 5, 10, 20$ and 40 were conducted for each scaling approach, with all initial conditions, mesh sizes and time steps scaled accordingly.

Table 4
Scaling laws for all WFSI relevant parameters under different scaling approaches.

Parameter	Unit	PFr	TFr_E	TFr	GP
H	m	λ	λ	λ	λ
T	s	$\lambda^{1/2}$	$\lambda^{1/2}$	$\lambda^{1/2}$	$\lambda^{1/2}$
ρ_w	kg/m^3	1	1	1	1
ν	m^2/s	$\lambda^{3/2}$	1	1	1
σ	N/m	λ^2	1	1	1
E	N/m^2	λ	λ	1	λ_E
ρ_s	kg/m^3	1	1	1	Unrestricted
s	m	λ	λ	λ	$\sqrt[3]{\lambda^4/\lambda_E}$
l	m	λ	λ	λ	λ
g	m/s^2	1	1	1	1

The precise Froude scaling (PFr) laws, in which the fluid and plate properties are correctly scaled (Catucci et al., 2021; 2023), were applied first. PFr do not involve any scale effects. Secondly, the traditional Froude–Cauchy scaling (TFr_E) laws, where ordinary water and air were used in the models, with the plate mechanical properties scaled according to Cauchy similarity, were employed. Scale effects in the TFr_E laws are due to the non conservation of Re, We and Ma.

Traditional Froude scaling (TFr, Catucci et al., 2021; 2023) laws were also applied, relying on ordinary water and air at reduced scales and the plate stiffness was unscaled. Scale effects in TFr are expected due to a non conservation of Re, We, Ma and Ca. Finally, a new scaling approach based on the WFSI dimensionless governing parameters (Table 3), referred to as GP, was used. This is based on the conservation of Π_1, Π_2, Π_6 and Π_7 between the prototype and models.

By assuming Π_1 and Π_2 to be constant between the prototype and models, the same scaling laws as under Froude scaling resulted for H and T (Table 4). For practical reasons, ordinary water and air were used in the models, such that Π_3 and Π_4 were not conserved, with a potential for scale effects. By introducing the E scaling law

$$\lambda_E = \frac{E_P}{E_M} \tag{9}$$

and assuming the conservation of Π_6 between the prototype and models,

$$s_M = \frac{s_P}{\sqrt[3]{\lambda^4/\lambda_E}} \tag{10}$$

results. This requires that λ_E is constant over the applied force range, such that the material response is linear or remains proportional between the prototype and models. Finally, it can be derived that l scales linearly with λ by imposing Π_7 to be constant between the prototype and models. The derived scaling laws for the GP approach are summarised in the last column of Table 4.

Based on this approach, the plate material in the models can be freely selected, λ_E can then be evaluated (Eq. (9)) and s can be estimated from Eq. (10). Acrylic plates ($E = 3.03$ GPa and $\rho_s = 1200$ kg/m^3) were used for the GP models of the present study, resulting in $\lambda_E = 66.01$ for $E_P = 200$ GPa. Note that Π_5 is intentionally not conserved in favour of a more versatile and practical approach. Consequently, no restrictions are applied to ρ_s, which otherwise would have to scale with $\sqrt[3]{\lambda_E/\lambda}$ to ensure $\Pi_{5,P} = \Pi_{5,M}$.

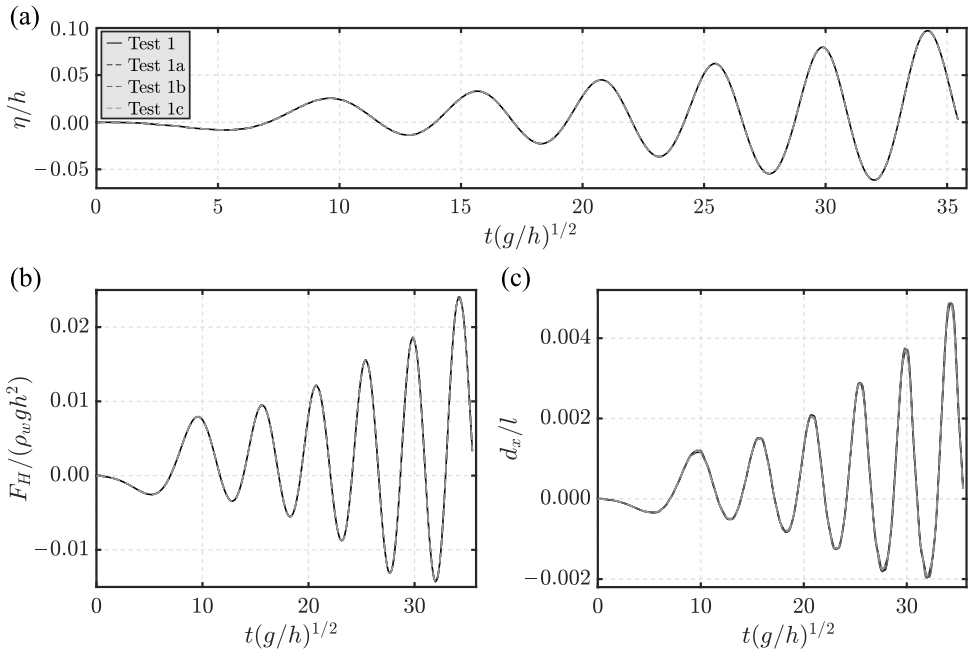

Fig. 2. Validation of the dimensionless governing parameters: dimensionless time histories of the (a) water surface elevations η/h at $x = 0$ m, (b) forces $F_H/(\rho_w g h^2)$ and (c) displacements d_x/l for the tests of Table 5.

Therefore, model effects (Kobus, 1980; Hughes, 1993) are expected due to an incorrect representation of the plate mass and need to be appropriately discussed (Section 4.2). These might be negligible in WFSI processes where the plate mass is of secondary importance in relation to its stiffness, as in the typical case of light-weight and slender structures under long-periodic waves where the structure dynamics is mainly controlled by the external loading.

3. Results

3.1. Validation of the governing parameters

The WFSI dimensionless governing parameters (Table 3) were validated herein, confirming their capability to fully capture the physics of WFSI. A regular wave prototype test (Section 2.1.2), referred to as test 1, was compared with 3 tests conducted under different conditions with the same parameters Π_1 to Π_7 (Table 5). In tests 1a and 1b, the set-up, fluid properties and the wave

Table 5
Test programme to validate the WFSI dimensionless parameters.

Symbol	Unit	Test 1	Test 1a	Test 1b	Test 1c
h	m	15	15	15	1
l	m	10	10	10	0.67
E	GPa	200	100	390	3
s	m	0.15	0.19	0.12	0.0165
ρ_s	kg/m^3	8000	6350	10000	4850
H	m	2	2	2	0.133
T	s	5.5	5.5	5.5	1.42
ν	m^2/s	$1.00 \cdot 10^{-6}$	$1.00 \cdot 10^{-6}$	$1.00 \cdot 10^{-6}$	$1.72 \cdot 10^{-8}$
σ	N/m	0.07	0.07	0.07	$3.11 \cdot 10^{-4}$
g	m/s^2	9.81	9.81	9.81	9.81
Π_1	–	0.13	0.13	0.13	0.13
Π_2	–	4.45	4.45	4.45	4.45
Π_3	–	$5.50 \cdot 10^{-9}$	$5.50 \cdot 10^{-9}$	$5.50 \cdot 10^{-9}$	$5.50 \cdot 10^{-9}$
Π_4	–	$3.17 \cdot 10^{-8}$	$3.17 \cdot 10^{-8}$	$3.17 \cdot 10^{-8}$	$3.17 \cdot 10^{-8}$
Π_5	–	0.08	0.08	0.08	0.08
Π_6	–	0.11	0.11	0.11	0.11
Π_7	–	0.67	0.67	0.67	0.67

features are identical to test 1. However, E in tests 1a is smaller than in test 1, with a larger s and smaller ρ_s. A thinner plate was used in test 1b, with both larger E and ρ_s compared to test 1.

Test 1c replicates an hypothetical, yet realistic, case at laboratory scale with $h = 1$ m. Consequently, H, T, ν, σ and l were evaluated by imposing the conservation of the corresponding $\Pi_1, \Pi_2, \Pi_3, \Pi_4$ and Π_7. By assuming $E = 3$ GPa, s was evaluated based on the conservation of Π_6 and consequently ρ_s was calculated from Π_5 (Table 5). In this test case, the mesh sizes and the time step were scaled to maintain the same spatial, e.g. $s/\Delta x$ and $l/\Delta z$, and temporal, e.g. $T/\Delta t$, resolutions as in test 1. The initial conditions were also scaled accordingly.

Fig. 2 shows the dimensionless water surface elevations η/h at $x = 0$ m, horizontal (subscript H) forces $F_H/(\rho_w g h^2)$ and horizontal displacements at the top end of the plate d_x/l for the 4 experiments of Table 5. The wave travelled along the flume and interacted with the plate, which oscillated with a period close to T. In the present study, $t = 0.0$ s is the instant when the first wave front reaches the plate and $F_H = F_{H,u} - F_{H,d}$, with the upwave (subscript u) $F_{H,u}$ and the downwave (subscript d) $F_{H,d}$ forces. The 4 experiments show identical results with less than 2% deviations. This confirms that the derived WFSI dimensionless governing parameters are able to represent the underlying physical processes of the phenomenon.

3.2. Non-breaking wave impacts

Scale effects are investigated in this section for the non-breaking wave tests (Table 2). Given the purpose of the present study, F_H and d_x at the top end of the plate were analysed. Further discussions of p and vertical stresses σ_{zz} are included in Section 4.2.

Figs. 3–5 show the time histories of the dimensionless F_H and d_x for the 3 prototype tests of Table 2 and the scaled models based on the approaches in Table 4. The PFr models are identical to the prototype, confirming full similarity. The TFr_E approach correctly

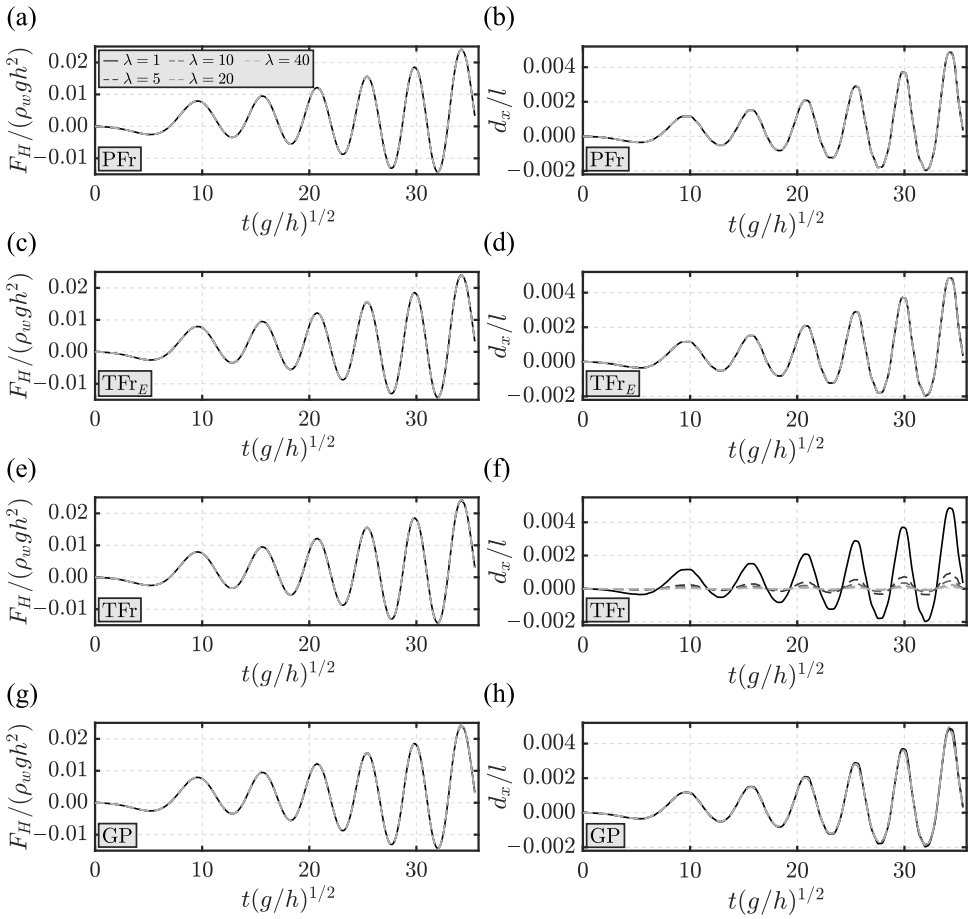

Fig. 3. Scale series for a regular wave test with $H/h = 0.13$ and $T(g/h)^{1/2} = 4.45$: dimensionless $F_H/(\rho_w g h^2)$ and d_x/l versus $t(g/h)^{1/2}$ for the prototype ($\lambda = 1$) and scaled models according to (a, b) PFr, (c, d) TFr_E, (e, f) TFr and (g, h) GP approaches.

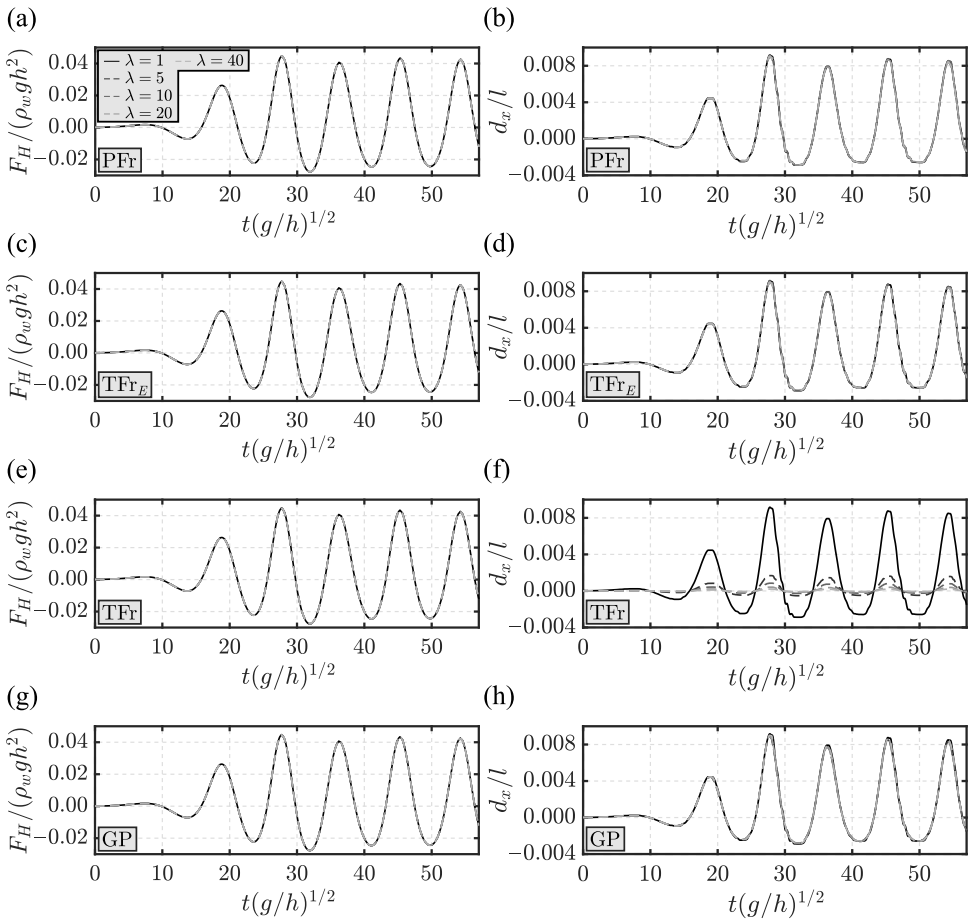

Fig. 4. Scale series for a regular wave test with $H/h = 0.13$ and $T(g/h)^{1/2} = 8.90$: dimensionless $F_H/(\rho_w g h^2)$ and d_x/l versus $t(g/h)^{1/2}$ for the prototype ($\lambda = 1$) and scaled models according to (a, b) PFr, (c, d) TFr_E, (e, f) TFr and (g, h) GP approaches.

scaled WFSI in all 3 tests, showing negligible Re, We and Ma scale effects (Figs. 3c, d, 4c, d and 5c, d). In the regular wave tests the plate oscillated with a period close to T. On the other hand, the plate showed faster oscillations following T_s (Table C.1) in the solitary wave test. In all tests, the plate oscillations were correctly captured in the PFr and TFr_E models. F_H were correctly modelled under TFr (Figs. 3e, 4e and 5e), however, d_x/l were underestimated by up to 97.8% (Figs. 3f, 4f and 5f) due to the unscaled E.

Finally, the scale series based on the new GP approach are shown in Figs. 3g, h, 4g, h and 5g, h. F_H were correctly predicted by the models, with less than 2.5% deviations compared to the prototype. The plate masses, hence the plate periods T_s (Table C.1), were incorrectly scaled introducing model effects. In these tests, $T_{s,M}$ are up to 58% smaller than the correctly scaled values $T_{s,M} = \lambda^{1/2} T_{s,P}$.

Although $T_{s,M}$ were inexact, the model plate dynamics were nearly identical to the prototype in all 3 tests, confirming that the plate motion is mostly controlled by the wave action in absence of resonance. In the regular wave tests, the frequency of the plate oscillations was correctly captured in the models (Figs. 3h and 4h). Deviations are observed at the peaks of d_x between the prototype and models, however, not exceeding 4.3% (Table C.2).

For the solitary wave tests, the models captured the main features of the plate deformation (Fig. 5h). The maximum (subscript *max*) $d_{x,max}/l$ in the models occurred slightly earlier in time compared to the prototype, with less than 3% deviations. However, the models were not able to capture the fastest oscillations shown in the prototype, particularly during wave run-down. Based on these findings, despite the deviations in the smaller frequency components of d_x, the GP approach predicted F_H and the overall plate deformation well. The scale effects addressed in this section are summarised in Table C.2 for each scaling approach and λ, including all 3 tests.

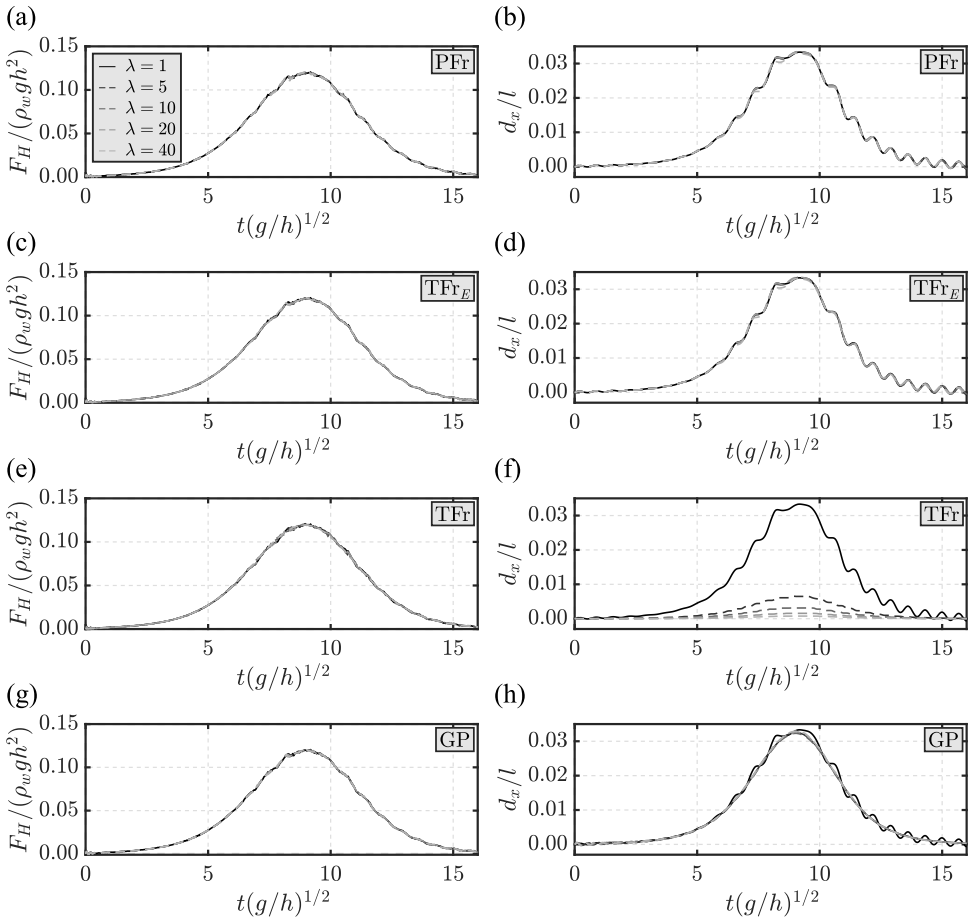

Fig. 5. Scale series for a solitary wave test with $a/h = 0.13$: dimensionless $F_H/(\rho_w g h^2)$ and d_x/l versus $t(g/h)^{1/2}$ for the prototype ($\lambda = 1$) and scaled models according to (a, b) PFr, (c, d) TFr$_E$, (e, f) TFr and (g, h) GP approaches.

3.3. Breaking wave impacts

Scaled breaking wave impacts on plates (Table 2) under TFr$_E$ laws are presented in this section. To be concise, only results from the flexible plate tests with $E_P = 200$ GPa and $s_P = 0.15$ m will be presented herein (Table 2). The wave pressures and forces from the scale series with $E_P = 400$ GPa and $s_P = 0.50$ m were similar to the flexible plate simulations and can be partially found in Section 4.3. In contrast to the non-breaking wave tests (Section 3.2), breaking wave impacts involve complex air–water interactions (Peregrine, 2003; Croquer et al., 2023) such that significant scale effects are expected. Note that both air and water are modelled as incompressible in solids4foam, as further discussed in Section 4.3.

Fig. 6a, b shows the time histories of $F_H/(\rho_w g h^2)$ and d_x/l (at the top end of the plate) for the prototype and its models. The first incident wave was reflected by the plate without breaking, resulting in a peak of $F_H/(\rho_w g h^2) = 0.16$ and $d_x/l = 0.006$ at $t(g/h)^{1/2} = 16.5$. Negligible scale effects can be observed at this stage, with $F_H/(\rho_w g h^2)$ and d_x/l accurately predicted at smaller model sizes.

The second wave broke before the impact, entrapping an air pocket (Fig. 7). This led to a violent impact with a sharp peak of F_H, followed by oscillations during run-up $27.7 \leq t/(g/h)^{1/2} \leq 29.2$. A further increase of F_H was observed at $t(g/h)^{1/2} = 30.2$ due to the collapse of the water column following the wave run-up (Linton et al., 2013; Didier et al., 2014; Attili et al., 2023).

These impact forces were incorrectly scaled under TFr$_E$, with significant Re, We and Ma scale effects (Fig. 6a). These effects can also be seen in Figs. 6c and 7, where the prototype and scaled wave impact $p/(\rho_w g h)$ for different snapshots are shown. Smaller model sizes tend to overpredict F_H and p (Cuomo et al., 2010b; Bredmose et al., 2015). As expected, the largest scale effects were observed at the smallest scale $\lambda = 40$, where F_H is up to twice the correctly scaled value. The air–water interfaces are inexactly modelled when air entrainment is important (Catucci et al., 2021); the models did not capture the complex free water surface observed for the prototype in detail. The shape, size and the pressures of the air pockets are also incorrectly scaled (Fig. 7).

The plate showed a peak of d_x due to the breaking wave impact at $t(g/h)^{1/2} = 28.05$, followed by a second peak corresponding to the collapse of the water column (Fig. 6b). After the wave was reflected, the plate oscillated with $T_s/(g/h)^{1/2} = 0.86$, being close

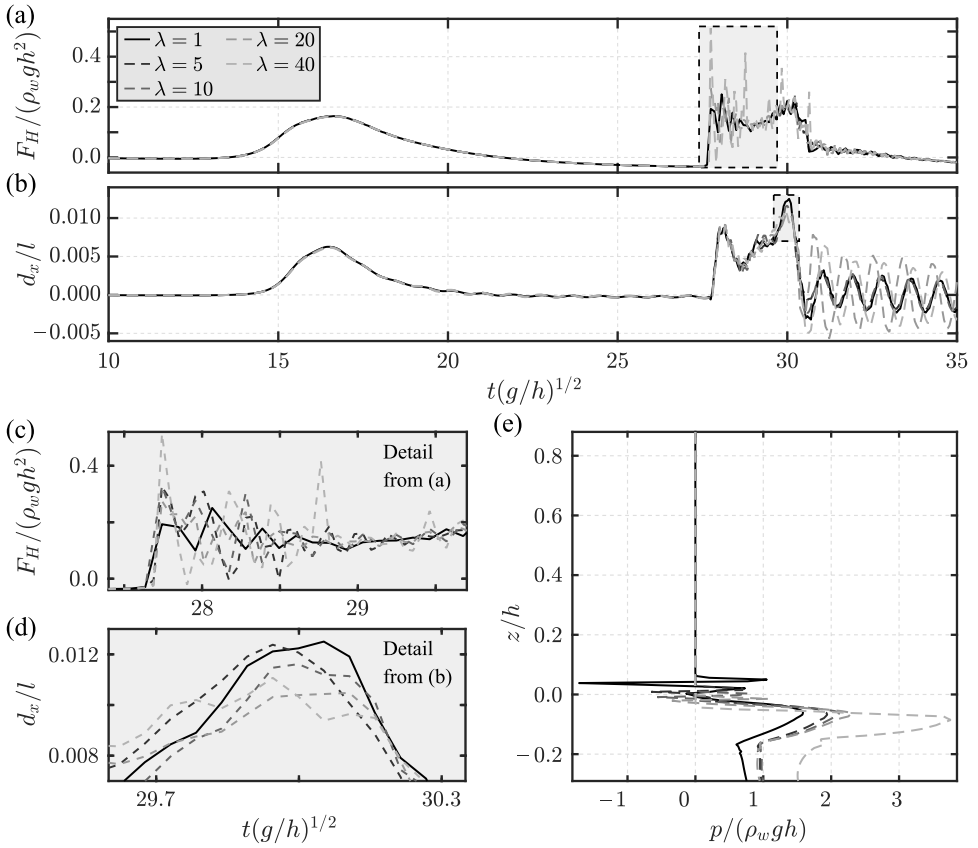

Fig. 6. Breaking wave impacts for the prototype ($\lambda = 1$) and scaled after TFr_E: time histories of the dimensionless (a) forces $F_H/(\rho_w g h^2)$ and (b) displacements d_x/l, with details of (c) $F_H/(\rho_w g h^2)$ and (d) d_x/l, and (e) pressure $p/(\rho_w g h)$ distribution at the plate at $t(g/h)^{1/2} = 27.7$.

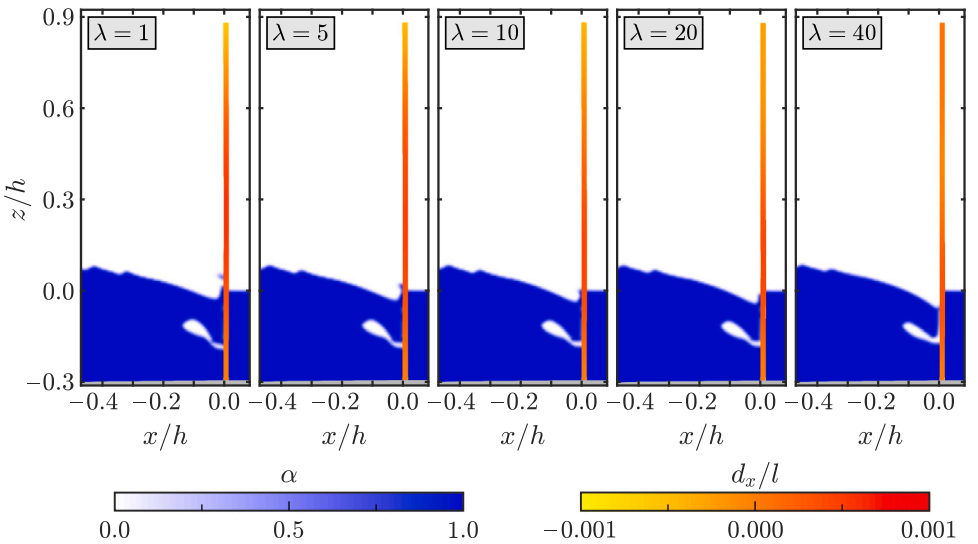

Fig. 7. Snapshots of breaking wave impact on the flexible plate at $t(g/h)^{1/2} = 27.7$ of the prototype ($\lambda = 1$) and TFr_E scaled models showing only minor scale effects.

to its natural period $T_s/(g/h)^{1/2} = 0.89$ (Gibson, 2007). As a consequence of the incorrect scaling of the breaking wave loading, the plate dynamics was not perfectly predicted by the models. The main differences concern the magnitude of the maximum peak, which is up to 17% underestimated by the models. Further, the d_x oscillations observed for $t(g/h)^{1/2} \geq 30.5$ were up to 2.5 times overpredicted at $\lambda = 20$ and 40, however, capturing their frequency correctly.

4. Discussion of results

4.1. Governing parameters

The governing parameters (Table 3) fully capture the underlying physical processes of WFSI (Fig. 2). These parameters can be used to define a range of physically-equivalent configurations, benefiting WFSI modelling, especially in laboratory scale models.

As an example, a prototype wood plate with $s = 0.15$ m, $E = 13$ GPa and $\rho_s = 1500$ kg/m^3 at $h = 20$ m is considered. For $\lambda = 10$, the TFr_E scaled model results in $s_M = 0.015$ m, $E_M = 1.3$ GPa and $\rho_{s,M} = 1500$ kg/m^3 at $h_M = 2$ m. Materials commonly used in the laboratory would not meet these requirements. However, based on the conservation of the WFSI governing parameters, a low density polyethylene plate with $s = 0.0237$ m, $E = 0.3$ GPa and $\rho_s = 950$ kg/m^3 can be used. This is physically-equivalent to the TFr_E scaled model, revealing the potential of the WFSI parameters to achieve plate similarity.

The 2D WFSI dimensionless parameters in Table 3 can be extended to Three-Dimensional (3D) phenomena, e.g. asymmetrical wave fields and/or curved structures. By introducing the 3D plate mass $M_{3D,s} = \rho_s sb$ and flexural rigidity $D_{3D} = Ebs^3/12$, with the plate width b, Π_5 and Π_6 for 3D were derived (Table 6). The remaining dimensionless parameters are identical to the 2D case. Due to the extensive computational cost, the 3D governing parameters were not validated, however, a similar behaviour as for the 2D case is expected (Fig. 2). This should be confirmed by future studies.

Table 6
Dimensionless governing parameters in 3D WFSI.

Π_1	Π_2	Π_3	Π_4	Π_5	Π_6	Π_7
$\frac{H}{h}$	$T(\frac{g}{h})^{1/2}$	$\frac{\nu}{g^{1/2}h^{3/2}}$	$\frac{\sigma}{\rho_w g h^2}$	$\frac{M_{3D,s}}{\rho_w h^2}$	$\frac{D_{3D}}{\rho_w g h^5}$	$\frac{l}{h}$

4.2. Scale effects in non-breaking waves

The investigated ranges of the main force ratios and WFSI dimensionless parameters are shown in Table C.3 for the non-breaking wave numerical tests (Section 3.2). Ca and Ma were computed as

$$\mathrm{Ca} = \frac{\rho_w g h}{E}, \tag{11}$$

$$\mathrm{Ma} = \frac{(gh)^{1/2}}{c_{sound}} \tag{12}$$

with the speed of sound in air $c_{sound} = (K_a/\rho_a)^{1/2}$ (Cramer, 1993), where K_a is the air (subscript a) bulk modulus. In the present study, $c_{sound} = 340$ m/s was assumed for the calculation of Ma. Although the air–water flows were modelled as incompressible, Ma is not conserved when ordinary water and air are used in the models due to the unscaled c_{sound}.

Non-breaking wave impacts on flexible plates were characterised by relatively small air–water interactions. The wave loading and plate behaviour were correctly scaled under the TFr_E approach, indicating that Re, We and Ma scale effects were relatively small in the investigated conditions (Table C.2). This is further confirmed by p and σ_{zz} in the TFr_E models, as shown in Fig. 8 for a representative test. It can be concluded that non-breaking wave impact pressures and forces are correctly scaled under traditional Froude similarity (Hughes, 1993; Cuomo et al., 2010b; Windt et al., 2021) and the plate dynamics are correctly predicted for accurately scaled plates.

On the other hand, significant scale effects for d_x were observed under TFr due to the unscaled E. The numerical $d_{x,M}$ (Figs. 3f, 4f and 5f) are upscaled by removing scale effects as (Fig. 9)

$$\frac{d_{x,P}}{l_P} = \frac{17}{16}\frac{\mathrm{Ca}_P}{\mathrm{Ca}_M}\frac{d_{x,M}}{l_M}, \tag{13}$$

with Ca calculated based on Eq. (11). Eq. (13) predicts the prototype plate displacements for incorrectly scaled models. However, it should be used for preliminary estimations only. Additional model effects due to the incorrect scaling of T_s might arise under TFr, which are not accounted for by Eq. (13) and need to be discussed on a case-by-case basis.

The new GP approach was also applied to scale non-breaking wave impacts. Acrylic plates were used in all the models to overcome the challenge of finding an appropriate material for scaled plates. Despite the inexact modelling of T_s, the GP models predicted the wave impact forces and plate displacements well (Figs. 3g, h, 4g, h and 5g, h). Scale effects due to the use of ordinary water and air in the models were negligible, as discussed for the TFr_E models. Based on the numerical observations, it can be concluded that this approach is suitable for WFSI with relatively small T/T_s, e.g. for regular waves or relatively stiff plates. In these cases, the GP approach predicts the prototype correctly, representing a valuable and more versatile alternative to TFr_E. On the other hand, non-negligible model effects might arise for larger T/T_s, e.g. for long period waves. In the solitary wave tests, the GP approach did not accurately predict the fastest frequency components of d_x, while providing satisfactory results for F_H and $d_{x,max}$ (Fig. 5g, h). Therefore, this approach can also be applied for relatively large T/T_s, if the main aim is to predict the maximum displacement, being significantly more versatile than the TFr_E approach.

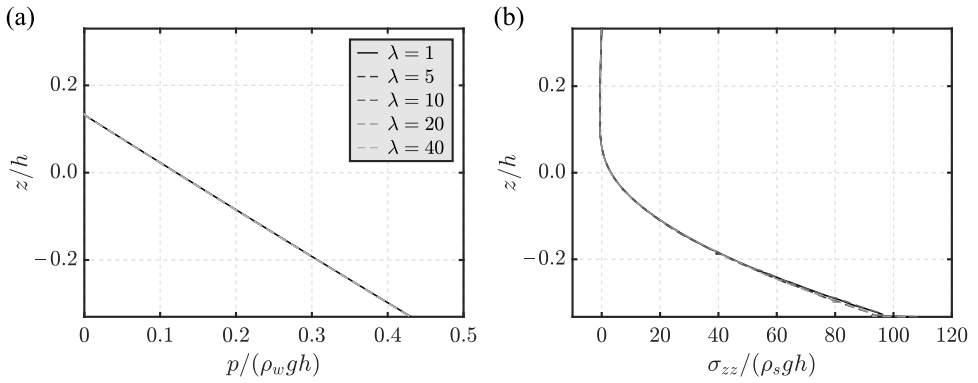

Fig. 8. Regular wave test with $H/h = 0.13$ and $T(g/h)^{1/2} = 8.90$: prototype and TFr_E scaled (a) $p/(\rho_w g h)$ versus z/h and (b) $\sigma_{zz}/(\rho_s g l)$ along the inner fibre (upwave) of the plate at the instant during $F_{H,max}$.

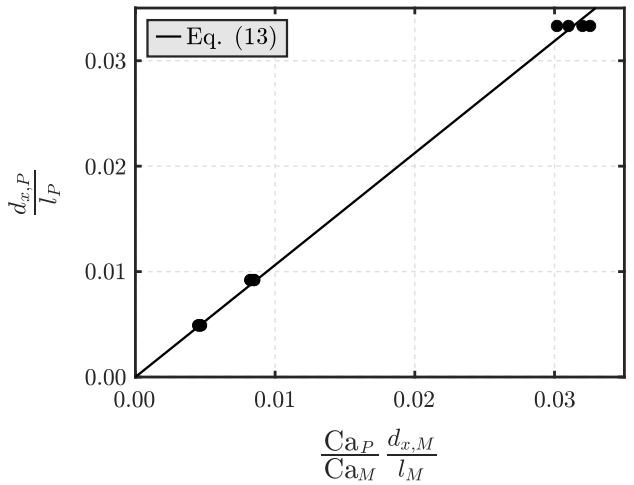

Fig. 9. Upscaling of d_x under TFr with Eq. (13) to remove scale effects: comparison of the numerical $\frac{d_{x,P}}{l_P}$ and predictions based on Eq. (13).

4.3. Scale effects in breaking waves

Relevant air–water interactions were observed for breaking waves impacting flexible plates (Section 3.3). The air–water compressibility may have a significant effect during wave impact, potentially resulting in reduced forces and pressures. However, the observed p_{max} were smaller than $3.18p_0$. Consequently, the air compression has a minor effect on the wave impact (Bredmose et al., 2015), such that the assumption of incompressible fluid in the simulation provides a suitable approximation. In addition, discrepancies of the numerical models from real observations do not affect the main conclusions of the present study as scale effects are quantified relative to numerical prototype observations.

By using ordinary water and air in the models, the TFr_E approach failed to correctly predict the prototype breaking wave impact (Figs. 6 and 7). The surface tension and air bulk modulus were overrepresented in the models, resulting in relatively smaller and stiffer air pockets at reduced scales (Cuomo et al., 2010b; Bredmose et al., 2015; Seiffert et al., 2015). At this stage, scale effects were predominantly due to We and Ma. On the other hand, stronger turbulence was observed at a later stage with the resurfacing of the air pocket such that Re effects are expected to be more significant. Fig. 10 shows the comparison of $p_{max,P}/p_{max,M}$ versus the dimensionless group $\frac{\mathrm{Re}_P}{\mathrm{Re}_M}\frac{\mathrm{We}_P}{\mathrm{We}_M}\frac{\mathrm{Ma}_P}{\mathrm{Ma}_M}$ along with the Froude scaling predictions. The largest scales, $\lambda = 5$ and 10, show relatively small deviations from the Froude scaling laws, however, up to 60% deviations are observed at $\lambda = 20$ and 40. The decreasing values of Re, We and Ma at smaller scales explain the observed deviations (Heller, 2011; 2017).

The numerical (subscript *num*) wave impact $p_{max,num}$ (Fig. 10) were upscaled with the approach of Cuomo et al. (2010b) (Section 1.1) removing scale effects. Table 7 shows the predicted (subscript *pred*) and numerical p_{max}/p_0 and $\lambda_p = p_M/p_P$ for both experimental conditions (Table 2). The method suggested by Cuomo et al. (2010b) agrees overall with the results of the present study

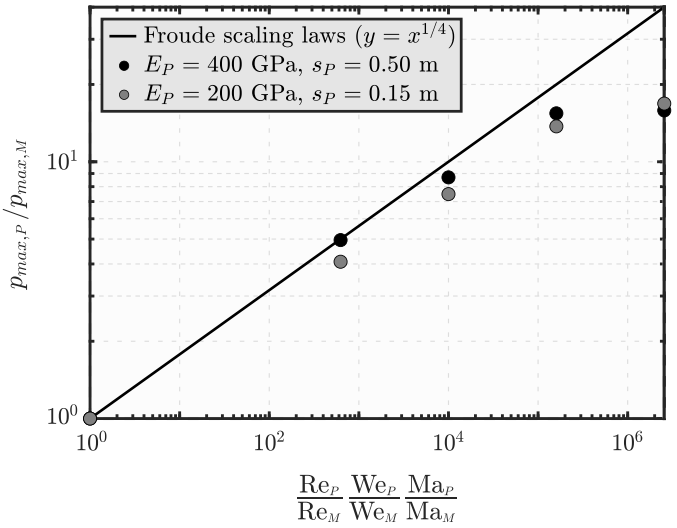

Fig. 10. Scale effects in wave breaking impacts: (–) prediction based on the Froude scaling laws and data of numerical relative impact pressures $p_{max,P}/p_{max,M}$ versus $\frac{\mathrm{Re}_P}{\mathrm{Re}_M}\frac{\mathrm{We}_P}{\mathrm{We}_M}\frac{\mathrm{Ma}_P}{\mathrm{Ma}_M}$.

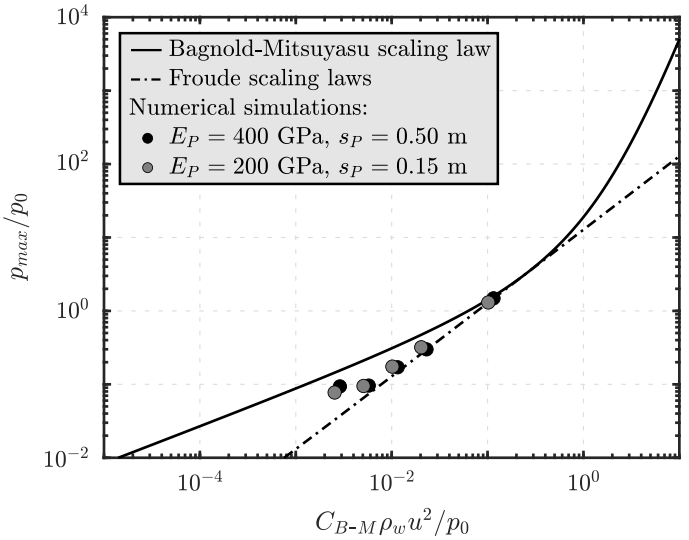

Fig. 11. Comparison of the numerical p_{max}/p_0 with the predictions based on the Bagnold–Mitsuyasu and the Froude scaling laws (after Bredmose et al., 2015).

in both experiments. For the stiffer plate, $\lambda_{p,pred}$ consistently underestimates the numerical observations with 23 to 26% deviations. Although this approach was developed for rigid walls, it captured the flexible plate results well, underestimating λ_p by only 12% at $\lambda = 5$, 10 and 20. Once again, $\lambda = 40$ shows the largest deviations.

Finally, the numerically derived pressure ratios p_{max}/p_0 are compared with the Bagnold–Mitsuyasu (Bredmose et al., 2015) and Froude scaling laws in Fig. 11. On the x-axis, the scale-invariant constant $C_{B\text{-}M}$ depends on the air pocket characteristics, e.g. the volume, and u is the fluid velocity. The x values for the prototype data points were determined from the Froude scaling laws at $p_{P,max}$ and then scaled with λ for the models (Bredmose et al., 2015). According to Bredmose et al. (2015), the Bagnold–Mitsuyasu model might not be accurate for $p_{max} \leq 3.18p_0$ due to the relatively stiffer air pockets. These tend to behave as rigid boundaries at such small scales, resulting in an overestimation of p. Consequently, the Froude scaling laws should be used for $p_{max} \leq 3.18p_0$. However, for $p_{max} > 3.18p_0$ the compression of the air pocket has a significant effect, such that the Bagnold–Mitsuyasu scaling law can be used to remove scale effects.

The numerical p_{max} lie between predictions based on the Bagnold–Mitsuyasu and Froude scaling laws (Fig. 11). These do not fully agree with the observations of Bredmose et al. (2015), particularly at the smallest scales. However, the air–water flows were modelled as incompressible in the present study, explaining the larger p compared to Bredmose et al. (2015). In addition, smaller values of Re, We and Ma were investigated in the present study, resulting in larger scale effects. This highlights once again the

Table 7
Comparison of the upscaled relative breaking wave impact pressures $p_{P,max}/p_0$ based on the approach of Cuomo et al. (2010b) with the numerical results of the present study, where $p_0 = 101.325$ kPa and $\Delta\lambda_p$ is the deviation between $\lambda_{p,pred}$ and $\lambda_{p,num}$.

	λ	$(p_{P,max,pred}/p_0)$	$(p_{max,num}/p_0)$	$\lambda_{p,pred}$	$\lambda_{p,num}$	$\Delta\lambda_p$
	1	–	1.48	–	–	–
	5	1.15	0.30	3.8	5.0	23%
$E_P = 400$ GPa	10	1.15	0.17	6.7	8.7	23%
$s_P = 0.50$ m	20	1.15	0.10	12.0	15.4	23%
	40	1.10	0.09	11.7	15.8	26%
	1	–	1.30	–	–	–
	5	1.15	0.32	3.6	4.1	12%
$E_P = 200$ GPa	10	1.15	0.17	6.6	7.5	12%
$s_P = 0.15$ m	20	1.15	0.09	12.1	13.7	12%
	40	0.85	0.08	12.9	16.9	23%

complexity of scale effects and the importance of taking the investigated force ratios into account, rather than λ only (Heller, 2011).

4.4. Upscaling of the laboratory tests

The laboratory measurements presented in Appendix B are used in this section as practical examples to discuss scale effects and to upscale the results to real-word cases. Based on the findings of Fig. B.2b and given that the waves did not break (Appendix B.2), scale effects due to Re, We and Ma are expected to be small. In addition, the laboratory Re $= 3.92 \cdot 10^5$, We $= 8.76 \cdot 10^3$ and Ma $= 4.61 \cdot 10^{-3}$ are within or close to the ranges investigated in Section 3.2 (Table C.3), indicating that scale effects are negligible.

By considering a hypothetical prototype scale with $h_P = 10.00$ m, $\lambda = 40$ results ($h_M = 0.25$, Table B.1). The upscaled parameters under TFr_E are shown in Table 8 for the rigid and flexible laboratory plates. A representative solitary wave with $a = 0.085$ m resulted in the 3D forces $F_{3D,H} = 56.09$ and 45.45 N on the vertical rigid and flexible laboratory plates. This corresponds to $a = 3.40$ m and $F_{3D,H} = 3589.76$ and 2908.80 kN on the rigid and flexible prototype plates, respectively.

Table 8
Upscaled laboratory test parameters of the rigid and flexible plate under the TFr_E and GP approaches, with $\lambda = 40$.

	Unit	Rigid plate (TFr_E)	Flexible plate (TFr_E)	Flexible plate (GP)
E_P	GPa	8000	132	200
$\rho_{s,P}$	kg/m^3	8000	1200	8000
s_P	m	0.12	0.16	0.14
l_P	m	22.00	22.00	22.00
b_P	m	9.60	9.60	9.60
h_P	m	10.00	10.00	10.00

Model effects due to the inexact scaling of the plate mass under GP are also expected to be negligible for the maximum wave force and plate deformation, as discussed in Sections 3.2 and 4.2. However, inaccurate predictions of the smaller frequency components of the plate dynamics might be expected in the upscaling of the solitary wave tests. Given the interest of the GP approach, only the flexible plate tests are discussed. In addition to $\lambda = 40$, λ_E needs to be defined. By assuming that the prototype is made of stainless steel ($E_P = 200$ GPa), λ_E is 60.6 based on $E_M = 3.3$ GPa. The prototype thickness can be calculated from Eq. (10), resulting in $s_P = 0.14$ m. At the prototype scale, solitary waves with a ranging from 0.84 to 3.40 m induce $F_{3D,H} = 449.35$ to 2908.80 kN, with up to $-5.73 \cdot 10^{-4}$ deformation along the centroid line of the plate. Regular waves with 0.565 m $\leq H \leq$ 1.642 m and 4.43 s $\leq T \leq$ 8.22 s, result in 144.17 kN $\leq F_{H,3D} \leq$ 563.80 kN and maximum strains of $\varepsilon_{zz} = -5.73 \cdot 10^{-4}$ to $-4.05 \cdot 10^{-5}$.

5. Conclusions

Scale effects have been rarely investigated in Wave–Structure Interaction (WSI) and may lead to incorrect predictions of the prototype behaviour. Free-surface flows are typically scaled according to the Froude scaling laws, involving scale effects when ordinary water and air are used in the models. For Wave–Flexible Structure Interaction (WFSI), the solid properties, e.g. the Young's modulus, must also be scaled based on Cauchy similarity. This can be difficult to achieve at reduced scale due to the challenge of finding a material with the appropriate properties, with potential for scale and model effects. A systematic investigation of scale effects in WSI was conducted in the present study. Regular and solitary wave impacts on rigid and flexible plates have been investigated at different scales based on numerical modelling supported by small-scale laboratory experiments. The main conclusions are summarised hereafter.

The 7 governing parameters Π_1 to Π_7 for WFSI (Table 3) have been derived and validated numerically (Fig. 2). These can be used to define physically-equivalent configurations at any scale. A new scaling approach was derived by conserving $\Pi_1 = H/h$, $\Pi_2 = T(g/h)^{1/2}$, $\Pi_6 = D/(\rho_w g h^4)$ and $\Pi_7 = l/h$ between the prototype and models, with the wave height H, wave period T,

water depth h, water density ρ_w, plate flexural rigidity D and the plate height l. This approach is more versatile than traditional Froude–Cauchy scaling (Section 2.3).

Non-breaking and breaking wave impacts have been simulated for 5 prototype tests (Table 2) and their models with geometrical scale factors $\lambda = 5, 10, 20$ and 40. These were scaled according to precise Froude (fluid and plate properties scaled), traditional Froude–Cauchy (fluid properties unscaled, plate properties scaled), traditional Froude (fluid and plate properties unscaled) and the new WFSI scaling approach. Accurate predictions of the prototype behaviour were achieved with precise Froude scaling. Traditional Froude–Cauchy scaling showed small scale effects for non-breaking waves. The wave pressures, forces and plate displacements were accurately predicted by the models with less than 2.1% deviations.

On the other hand, significant scale effects were observed for breaking wave impacts under traditional Froude–Cauchy similarity (Fig. 6). The models incorrectly predict the prototype behaviour due to the unscaled fluid properties. The wave pressures were overestimated by up to 132% at smaller scales with $\lambda = 40$. The scaled pressures resulted in a reasonable agreement with available approaches (Cuomo et al., 2010b; Bredmose et al., 2015), removing scale effects in the upscaling of breaking wave impacts on rigid plates. Smaller discrepancies were explained by the assumption of incompressible fluids and the smaller values of the Reynold, Weber and Mach numbers used in the present study (Section 4.3).

Traditional Froude scaling showed significant scale effects due to the unscaled plate properties (Figs. 3f, 4f and 5f). These resulted in an up to 98% underestimation of the plate displacements at $\lambda = 40$. Scale effects can be removed in the upscaling of the plate displacements with the newly proposed Eq. (13).

The new scaling approach based on the WFSI governing parameters was successfully validated with non-breaking waves. The regular wave models showed accurately scaled wave pressures, forces and plate displacements, with less than 4.3% deviations (Figs. 3g, h and 4g, h). The solitary wave tests revealed that, despite non-negligible model effects due to the non conservation of T relative to the plate period T_s, the wave loadings and plate dynamics were predicted reasonably well (Fig. 5g, h). The maximum solitary wave force and plate displacement showed less than 3% deviations. While being more versatile than traditional Froude–Cauchy scaling laws, this approach is suitable for relatively small and large ratios of T/T_s, i.e. if the plate mass effects are small. However, this approach may not be appropriate for other WFSI processes where the inertia of the structure plays a significant role, such as for offshore floating platforms or offshore pipelines.

Future work should validate the new scaling approach in laboratory experiments and in other WFSI processes. This would also provide insight in related model effects.

CRediT authorship contribution statement

Tommaso Attili: Formal analysis, Investigation, Methodology, Validation, Visualization, Writing – original draft, Writing – review & editing. **Valentin Heller:** Conceptualization, Funding acquisition, Methodology, Project administration, Supervision, Validation, Writing – review & editing. **Savvas Triantafyllou:** Conceptualization, Methodology, Supervision, Validation, Writing – review & editing.

Declaration of competing interest

The authors declare that they have no known competing financial interests or personal relationships that could have appeared to influence the work reported in this paper.

Data availability

Data will be made available on request.

Acknowledgements

The authors would like to thank Dr. Ricardo Correia and Dr. Sándor Erdődy from the Optics and Photonics Group for providing the fibre optic sensors used in the laboratory tests. Dr. Walid Tizani from the Centre for Structural Engineering & Informatics is acknowledged for lending the interrogator for the laboratory tests. Mr. Sam Cook and Mr. Alistair Palmer are acknowledged for supporting the experimental design and for helping with the measurement equipment for the laboratory experiments. The Ph.D. study of Tommaso Attili was financially supported by the University of Nottingham Vice-Chancellor's Scholarship for Research Excellence. The third author acknowledges the support of the European Union's Horizon research and innovation programme under the Marie Sklodowska-Curie Individual Fellowship grant "AI2AM: Artificial Intelligence driven topology optimisation of Additively Manufactured composite components", No. 101021629. The simulations were conducted on the HPC cluster Augusta at the University of Nottingham.

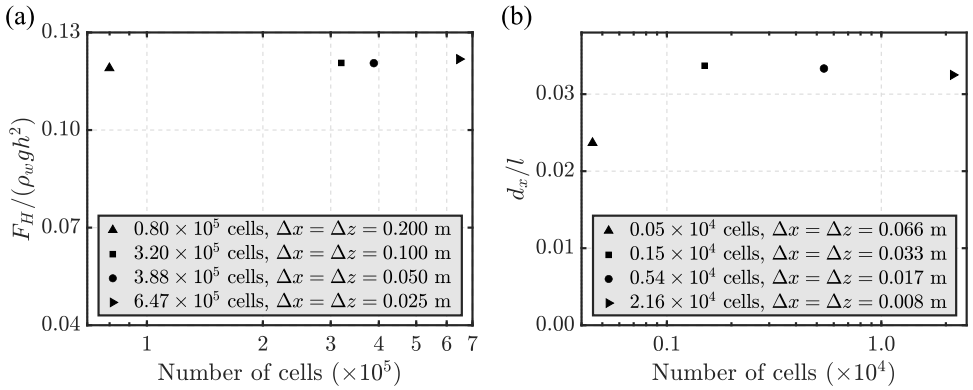

Fig. A.1. Convergence tests for a solitary non-breaking wave test with $a/h = 0.13$: semi-logarithmic diagram for the relative (a) force $F_H/(\rho_w g h^2)$ and (b) horizontal displacement d_x/l with the mesh size $\Delta x = \Delta z$.

Appendix A. Convergence tests

Fig. A.1 shows the convergence tests for a non-breaking solitary wave test (Fig. 1a). Mesh resolutions of $\Delta x = \Delta z = 0.200, 0.100, 0.050$ and 0.025 m were investigated for the fluid domain. The finest resolutions $\Delta x = \Delta z = 0.050$ and 0.025 m were employed in a 11 m × 22 m refined area only, while $\Delta x = \Delta z = 0.10$ m was used in the remainder of the fluid domain. Convergence is achieved for $\Delta x = \Delta z = 0.05$ m, which was selected for the main tests. This showed deviations of only 1% compared to the finest resolutions, while requiring approximately 1/5 of the computational time.

Resolutions of $\Delta x = \Delta z = 0.066, 0.033, 0.017$ and 0.008 m were investigated for the plate. $\Delta x = \Delta z = 0.017$ m was selected as the optimal mesh size for the main tests. This resulted in a 2.4% larger d_x/h compared to $\Delta x = \Delta z = 0.008$ m, while saving computational time.

Appendix B. Physical model

B.1. Laboratory set-up

Laboratory tests were conducted in a 15.0 m long, 0.245 m wide and 0.460 deep flume (Fig. B.1a). The flume was equipped with a piston-type wave maker. A 0.55 m × 0.24 m plate was located approximately 11.50 m downwave the wave maker. The plate was supported by a movable angled ramp to vary the plate inclinations β. A 2.0 to 2.5 mm gap between the plate and the lateral walls of the flume ensured a free movement of the plate.

Resistance-type Wave Gauges (WGs) were used at 3 locations to record water surface elevations. They sampled at 100 Hz with ±1 mm accuracy. Water pressures on the plate were measured with an array of MPXV5004GC7U (RS Components UK) Precision Pressure Transducers (PPTs), which recorded at 100 Hz with an estimated accuracy of ±10 Pa. In-house Load Cells (LCs) were mounted at the corners of the plate to measure the wave forces on the plate. Forces were recorded at 1 kHz with an overall accuracy of ±0.3 N. Finally, KFWB Series Waterproof Strain Gauges (SGs) were glued to the flexible plate to measure deflections.

A total of 52 laboratory tests were conducted with $h = 0.25$ m. These involved a range of regular and solitary waves impacting a stainless steel ($E = 200.0$ GPa) and an acrylic ($E = 3.3$ GPa) plate with $\beta = 60$ and 90°. The laboratory test programme is summarised in Table B.1.

B.2. Laboratory results

Fig. B.2a shows the horizontal 3D forces $F_{3D,H}$ versus a/h for the laboratory tests of Table B.1. The flexible plate resulted overall in smaller forces than the rigid one. This effect was larger for $\beta = 90°$ than for $\beta = 60°$, with up to 29% deviations of $F_{3D,H}$ between $E = 3.30$ and 200 GPa. The laboratory $F_{3D,H}$ were approximated as (Fig. B.2b)

$$\frac{F_{3D,H}}{\rho_w g h^3} = \left(\frac{a}{h}\right)^{7/6} \Pi_6^{1/12} \left(\frac{\beta}{90°}\right)^{1/3}, \tag{B.1}$$

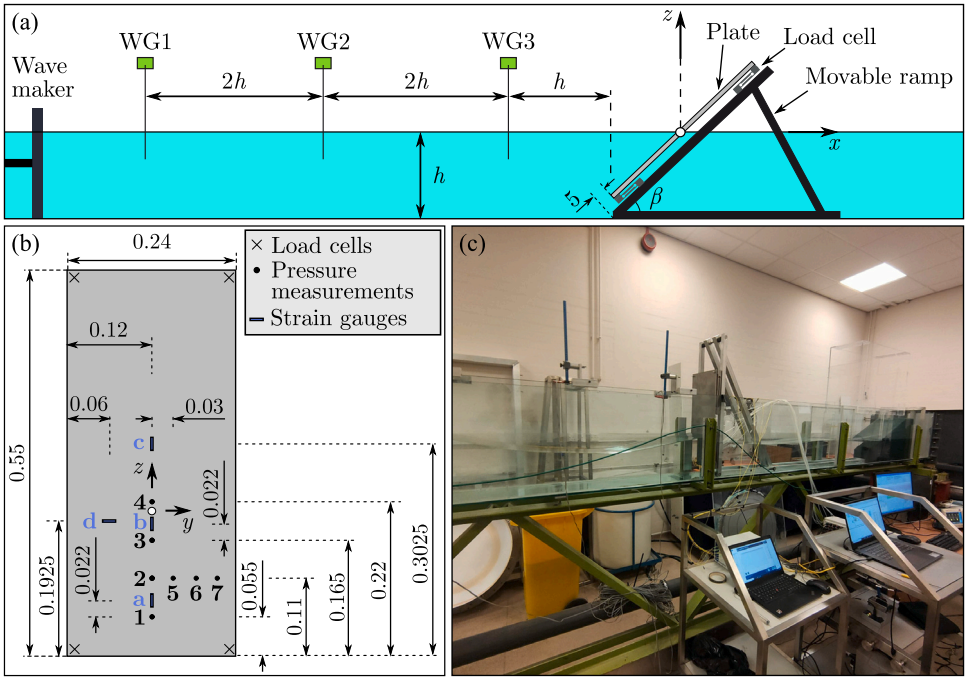

Fig. B.1. Laboratory set-up: (a) schematic side view of the wave flume and plate, (b) frontal view of the plate with location of the measurement systems and (c) picture of the wave flume with some of the instrumentation (Attili et al., 2023).

Table B.1
Test programme for the laboratory tests.

Parameter	Symbol	Unit	Range
Water depth	h	m	0.25
Plate height	l	m	0.55
Plate width	b	m	0.24
Plate inclination	β	°	60, 90
Young's modulus	E	GPa	3.30, 200.00
Plate thickness	s	m	0.003, 0.004
Plate density	ρ_s	kg/m^3	1190, 8000
Regular waves	H	m	0.014 to 0.041
	H/h	–	0.056 to 0.164
	T	s	0.7 to 1.3
	$T(g/h)^{1/2}$	–	4.39 to 8.14
Solitary waves	a	m	0.021 to 0.085
	a/h	–	0.084 to 0.34

based on a least-squares regression analysis. Data points from the 3 numerical non-breaking wave prototype tests (Table 2) are shown in Fig. B.2b along with Eq. (B.1) and the laboratory $F_{3D,H}$. The 2D numerical F_H were multiplied by λb_M to obtain $F_{3D,H}$, with the laboratory plate width $b_M = 0.24$ m and $\lambda = 60$. Despite the differences between the set-ups and the plate support conditions (Figs. 1a and B.1), the dimensionless numerical and laboratory $F_{3D,H}$ show similar values. This is a strong indication that scale effects are negligible in these laboratory experiments (Section 4.4).

The maximum strain ϵ_{zz} measured at the upwave Strain Gauge b (SGb, Fig. B.1b) are shown in Fig. B.2c. Note that the initial deformations due to the weight of the plate have been deducted. Larger ϵ_{zz} resulted from larger a/h following a linear trend. These

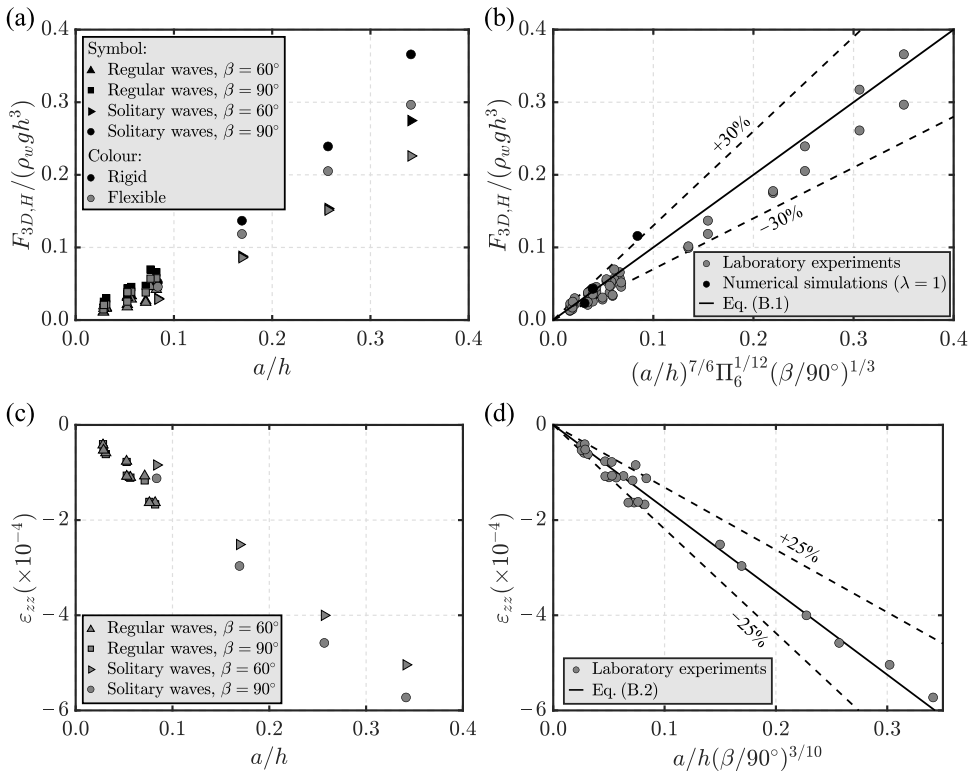

Fig. B.2. Laboratory experiments: (a) maximum relative forces $F_{3D,H}/(\rho_w g h^3)$ versus a/h for all tests of Table B.1, (b) $F_{3D,H}/(\rho_w g h^3)$ with Eq. (B.1) (coefficient of determination $R^2 = 0.98$) and the data points of the non-breaking wave prototype ($\lambda = 1$) numerical tests (Table 2), (c) maximum ε_{zz} at SGb versus a/h for the flexible plate ($E = 3.30$ GPa) tests and (d) ε_{zz} at SGb with Eq. (B.2) ($R^2 = 0.98$).

were approximated as (Fig. B.2d)

$$\varepsilon_{zz} = \frac{14}{8} \cdot 10^{-3} \frac{a}{h} \left(\frac{\beta}{90°} \right)^{3/10}. \tag{B.2}$$

As shown in Fig. B.2d, Eq. (B.2) captures the laboratory observations well, with most data lying within the ±25% limits.

Appendix C. Supplementary tables

Tables C.1 to C.3 include some data in support of the main part of the article.

Table C.1
Natural plate period $T_s = [2\pi l^2/1.875^2]\sqrt{12\rho_s/(Es^2)}$ (Gibson, 2007) and dimensionless plate period $T_s(g/h)^{1/2}$ for the non-breaking wave tests of Table 2 under the scaling approaches shown in Table 4.

		$\lambda = 1$	$\lambda = 5$	$\lambda = 10$	$\lambda = 20$	$\lambda = 40$
PFr	T_s (s)	0.83	0.37	0.26	0.18	0.13
	$T_s(g/h)^{1/2}$ (-)	0.67	0.67	0.67	0.67	0.67
TFr_E	T_s (s)	0.83	0.37	0.26	0.18	0.13
	$T_s(g/h)^{1/2}$ (-)	0.67	0.67	0.67	0.67	0.67
TFr	T_s (s)	0.83	0.17	0.08	0.04	0.02
	$T_s(g/h)^{1/2}$ (-)	0.67	0.30	0.21	0.15	0.11
GP	T_s (s)	0.83	0.22	0.14	0.09	0.05
	$T_s(g/h)^{1/2}$ (-)	0.67	0.40	0.35	0.32	0.28

Table C.2
Scale effects $\Delta F_{H,max}$ and $\Delta d_{x,max}$ for the maximum force and displacement, respectively, for the non-breaking wave tests of Table 2 under the scaling approaches shown in Table 4.

	$\lambda = 5$	$\lambda = 10$	$\lambda = 20$	$\lambda = 40$
PFr	$\Delta F_{H,max} < 1.0\%$ $\Delta d_{x,max} < 2.0\%$	$\Delta F_{H,max} < 1.0\%$ $\Delta d_{x,max} < 1.0\%$	$\Delta F_{H,max} < 1.0\%$ $\Delta d_{x,max} < 1.5\%$	$\Delta F_{H,max} < 1.0\%$ $\Delta d_{x,max} < 1.5\%$
TFr_E	$\Delta F_{H,max} < 1.0\%$ $\Delta d_{x,max} \leq 2.1\%$	$\Delta F_{H,max} < 1.0\%$ $\Delta d_{x,max} < 1.0\%$	$\Delta F_{H,max} < 1.0\%$ $\Delta d_{x,max} < 2.0\%$	$\Delta F_{H,max} < 1.0\%$ $\Delta d_{x,max} < 2.0\%$
TFr	$\Delta F_{H,max} < 1.0\%$ $80.4\% \leq \Delta d_{x,max} \leq 81.7\%$	$\Delta F_{H,max} < 1.0\%$ $90.4\% \leq \Delta d_{x,max} \leq 90.8\%$	$\Delta F_{H,max} < 1.0\%$ $95.3\% \leq \Delta d_{x,max} \leq 95.5\%$	$\Delta F_{H,max} \leq 1.0\%$ $97.7\% \leq \Delta d_{x,max} \leq 97.8\%$
GP	$\Delta F_{H,max} < 1.0\%$ $1.0\% \leq \Delta d_{x,max} \leq 3.4\%$	$\Delta F_{H,max} < 1.0\%$ $2.5\% \leq \Delta d_{x,max} \leq 4.3\%$	$\Delta F_{H,max} \leq 2.5\%$ $1.9\% \leq \Delta d_{x,max} \leq 3.8\%$	$\Delta F_{H,max} \leq 1.4\%$ $1.0\% \leq \Delta d_{x,max} \leq 2.4\%$

Table C.3
Ranges of Re, We, Ma, Ca and WFSI dimensionless parameters investigated in the non-breaking wave impact tests for different scaling approaches.

	Re	We	Ma	Ca
PFr	$1.82 \cdot 10^8$	$3.15 \cdot 10^7$	$3.57 \cdot 10^{-2}$	$7.36 \cdot 10^{-7}$
TFr_E	$7.19 \cdot 10^5$ to $1.82 \cdot 10^8$	$1.97 \cdot 10^4$ to $3.15 \cdot 10^7$	$5.64 \cdot 10^{-3}$ to $3.57 \cdot 10^{-2}$	$7.36 \cdot 10^{-7}$
TFr	$7.19 \cdot 10^5$ to $1.82 \cdot 10^8$	$1.97 \cdot 10^4$ to $3.15 \cdot 10^7$	$5.64 \cdot 10^{-3}$ to $3.57 \cdot 10^{-2}$	$1.84 \cdot 10^{-8}$ to $7.36 \cdot 10^{-7}$

	Π_1	Π_2	Π_3	Π_4	Π_5	Π_6	Π_7
GP	0.13	4.45 to 8.90	$5.50 \cdot 10^{-9}$ to $1.39 \cdot 10^{-6}$	$3.17 \cdot 10^{-8}$ to $5.07 \cdot 10^{-5}$	0.0142 to 0.08	0.113	0.67

References

Abrahamsen, B.C., Faltinsen, O.M., 2013. Scaling of entrapped gas pocket slamming events at dissimilar Euler number. J. Fluids Struct. 40, 246–256.

Abrahamsen, B.C., Grytten, F., Hellan, Ø., Søreide, T.H., Faltinsen, O.M., 2023. Hydroelastic response of concrete shells during impact on calm water. J. Fluids Struct. 116, 103804.

Attili, T., Heller, V., Triantafyllou, S., 2021. A numerical investigation of tsunamis impacting dams. Coast. Eng. 169, 103942.

Attili, T., Heller, V., Triantafyllou, S., 2022. Numerical investigation of impulse waves impacting dams. In: 39th International Association for Hydro-Environmental Engineering and Research World Congress. pp. 2222–2229.

Attili, T., Heller, V., Triantafyllou, S., 2023. Wave impact on rigid and flexible plates. Coast. Eng. 182, 104302.

Blenkinsopp, C.E., Chaplin, J.R., 2011. Void fraction measurements and scale effects in breaking waves in freshwater and seawater. Coast. Eng. 58 (5), 417–428.

Brackbill, J.U., Kothe, D.B., Zemach, C., 1992. A continuum method for modeling surface tension. J. Comput. Phys. 100 (2), 335–354.

Bredmose, H., Bullock, G.N., Hogg, A.J., 2015. Violent breaking wave impacts. Part 3. Effects of scale and aeration. J. Fluid Mech. 765, 82–113.

Buckingham, E., 1914. On physically similar systems - illustrations of the use of dimensional equations. Phys. Rev. 4 (4), 345–376.

Cardiff, P., Karač, A., Jaeger, P.D., Jasak, H., Nagy, J., Ivanković, A., Tuković, Z., 2018. An open-source finite volume toolbox for solid mechanics and fluid-solid interaction simulations. ArXiv Prepr ArXiv:180810736.

Catucci, D., Briganti, R., Heller, V., 2021. Numerical validation of novel scaling laws for air entrainment in water. Proc. R. Soc. A: Math. Phys. Eng. Sci. 477 (2255), 20210339.

Catucci, D., Briganti, R., Heller, V., 2023. Numerical validation of novel scaling laws for air-water flows including compressibility and heat transfer. J. Hydraul. Res. 61 (4), 517–531.

Chakrabarti, S.K., 2005. Offshore structure modeling. Elsevier, London, UK.

Chanson, H., Aoki, S., Hoque, A., 2004. Physical modelling and similitude of air bubble entrainment at vertical circular plunging jets. Chem. Eng. Sci. 59 (4), 747–758.

Courant, R., Friedrichs, K., Lewy, H., 1928. Über die partiellen Differenzengleichungen der Mathematischen Physik. Math. Ann. 100, 32–74.

Cramer, O., 1993. The variation of the specific heat ratio and the speed of sound in air with temperature, pressure, humidity, and CO2 concentration. J. Acoust. Soc. Am. 93 (5), 2510–2516.

Croquer, S., Díaz-Carrasco, P., Tamimi, V., Poncet, S., Lacey, J., Nistor, I., 2023. Modelling wave–structure interactions including air compressibility: A case study of breaking wave impacts on a vertical wall along the Saint-Lawrence Bay. Ocean Eng. 273, 113971.

Cuomo, G., Allsop, W., Bruce, T., Pearson, J., 2010a. Breaking wave loads at vertical seawalls and breakwaters. Coast. Eng. 57 (4), 424–439.

Cuomo, G., Allsop, W., Takahashi, S., 2010b. Scaling wave impact pressures on vertical walls. Coast. Eng. 57 (6), 604–609.

Didier, E., Neves, D., Martins, R., Neves, M., 2014. Wave interaction with a vertical wall: SPH numerical and experimental modeling. Ocean Eng. 88, 330–341.

Erbisti, P., 2014. Design of Hydraulic Gates. Balkema, Lisse, Netherlans.

Falcão, A.F., Henriques, J.C., 2014. Model-prototype similarity of oscillating-water-column wave energy converters. Int. J. Mar. Energy 6, 18–34.

Gibson, R.F., 2007. Principles of Composite Material Mechanics. CRC press, Florida.

He, G., Kashiwagi, M., 2012. Numerical analysis of the hydroelastic behavior of a vertical plate due to solitary waves. J. Mar. Sci. Technol. 17 (2), 154–167.

Heller, V., 2011. Scale effects in physical hydraulic engineering models. J. Hydraul. Res. 49 (3), 293–306.

Heller, V., 2017. Self-similarity and Reynolds number invariance in Froude modelling. J. Hydraul. Res. 55 (3), 293–309.

Heller, V., Hager, W.H., Minor, H.-E., 2008. Scale effects in subaerial landslide generated impulse waves. Exp. Fluids 44 (5), 691–703.

Hirt, C.W., Nichols, B.D., 1981. Volume of fluid (VOF) method for the dynamics of free boundaries. J. Comput. Phys. 39 (1), 201–225.

Hudson, R.Y., Herrmann, F.A., Sager, R.A., 1979. Coastal Hydraulic Models (Technical Report). US Army Engineer Waterways Experiment Station, Vicksburg, Mississippi.

Hughes, S.A., 1993. Physical Models and Laboratory Techniques in Coastal Engineering. World Scientific, Singapore.

Jacobsen, N.G., Fuhrman, D.R., Fredsøe, J., 2012. A wave generation toolbox for the open-source CFD library: OpenFOAM. Internat. J. Numer. Methods Fluids 70 (9), 1073–1088.

Kiger, K.T., Duncan, J.H., 2012. Air-entrainment mechanisms in plunging jets and breaking waves. Annu. Rev. Fluid Mech. 44 (1), 563–596.

Kobus, H., 1980. Hydraulic Modelling. German Association for Water Resources and Land Improvement (Bulletin 7), Hamburg, Germany.

Krautwald, C., von Häfen, H., Niebuhr, P., Vögele, K., Stolle, J., Schimmels, S., Schürenkamp, D., Sieder, M., 2022. Collapse processes and associated loading of square light-frame timber structures due to bore-type waves. Coast. Eng. 177, 104178.
Lagoun, M.S., Benalia, A., Benbouzid, M.E.H., 2010. Ocean wave converters: State of the art and current status. In: 2010 IEEE International Energy Conference. pp. 636–641.
Lambert, S., Bourrier, F., Ceron-Mayer, A.R., Dugelas, L., Dubois, F., Piton, G., 2023. Small-scale modeling of flexible barriers. I: Mechanical similitude of the structure. J. Hydraulic Eng. 149, 04022043.
Launder, B., Spalding, D., 1974. The numerical computation of turbulent flows. Comput. Methods Appl. Mech. Engrg. 3 (2), 269–289.
Le Méhauté, B., 1965. On Froude-Cauchy similitude. In: Proceedings Santa Barbara specialty conference. pp. 327–345.
Le Méhauté, B., 1976. An Introduction to Hydrodynamics and Water Waves. Springer, New York.
Le Méhauté, B., 1990. Similitude. Ocean engineering science: The sea. Wiley, New York, pp. 955–980,
Linton, D., Gupta, R., Cox, D., van de Lindt, J., Oshnack, M.E., Clauson, M., 2013. Evaluation of tsunami loads on wood-frame walls at full scale. J. Struct. Eng. 139 (8), 1318–1325.
Liu, M., Zhang, Z., 2019. Smoothed particle hydrodynamics (SPH) for modeling fluid-structure interactions. Sci. China Phys. Mech. Astron. 62 (8), 984701.
Martinelli, L., Lamberti, A., Gaeta, M.G., Tirindelli, M., Alderson, J., Schimmels, S., 2011. Wave loads on exposed jetties: Description of large scale experiments and preliminary results. Coast. Eng. Proc. 1 (32).
OpenFOAM extension, 2016. https://sourceforge.net/u/hjasak/foam-extend-4.0/ci/master/tree/. (Accessed: 26 September 2023).
Oumeraci, H., 1984. Scale effects in coastal hydraulic models. In: Symposium on Scale Effects in Modelling Hydraulic Structures. pp. 7–10.
Peregrine, D.H., 2003. Water-wave impact on walls. Annu. Rev. Fluid Mech. 35 (1), 23–43.
Seiffert, B.R., Ertekin, R.C., Robertson, I.N., 2015. Wave loads on a coastal bridge deck and the role of entrapped air. Appl. Ocean Res. 53, 91–106.
Sheng, W., Alcorn, R., Lewis, T., 2014. Physical modelling of wave energy converters. Ocean Eng. 84, 29–36.
Tuković, Z., Karač, A., Cardiff, P., Jasak, H., Ivanković, A., 2018. OpenFOAM finite volume solver for fluid-solid interaction. Trans. FAMENA 42, 1–31.
Windt, C., Davidson, J., Ringwood, J.V., 2021. Numerical analysis of the hydrodynamic scaling effects for the Wavestar wave energy converter. J. Fluids Struct. 105, 103328.